Nano Energy 108 (2023) 108193

Contents lists available at ScienceDirect

Nano Energy

journal homepage: www.elsevier.com/locate/nanoen

Reduction-tolerant SnO_2 assisted by surface hydroxyls for selective CO_2 electroreduction to formate over wide potential range

Zhipeng Liu [a,b], Junjie Chen [c], Hongshan Guo [a], Xiaoxi Huang [a,*]

[a] Hoffmann Institute of Advanced Materials, Postdoctoral Innovation Practice Base, Shenzhen Polytechnic, 7098 Liuxian Blvd, Nanshan District, Shenzhen 518055, PR China
[b] Shenzhen Institutes of Advanced Technology, Chinese Academy of Sciences, Shenzhen 518055, PR China
[c] State Key Laboratory of Supramolecular Structures and Materials, Jilin University, 2699 Qianjin Avenue, Changchun, PR China

ARTICLE INFO

Keywords:
CO_2 reduction reaction
Tin dioxide
Surface hydroxyls
Formate
Electrocatalyst

ABSTRACT

Tin oxide based materials have been identified as active catalysts for electrochemical CO_2-to-formate conversion. However, the oxide is unstable and can easily reconstruct via self-reduction under CO_2 reduction reaction (CO_2RR) condition, resulting in undesired elevated hydrogen evolution reactivity. In this work, a stable tin dioxide (SnO_2-1) electrocatalyst with abundant surface hydroxyls was synthesized via sodium cation assisted calcination method. The resulting electrocatalyst exhibits higher selectivity toward formate in a wide potential window compared with the one with very little hydroxyl groups. In addition, we demonstrate that SnO_2-1 can operate at high current density of 200 $mA{\cdot}cm^{-2}$ for at least 6 h while maintaining $FE_{formate}$ over 80%. Assisted with density functional theory (DFT) calculations, we propose that the presence of surface hydroxyls factors significantly into the overall performance of CO_2RR, including optimization of the formation energy of key intermediate *OCHO and help SnO_2 to preserve partially reduced active surface.

1. Introduction

Climate change and energy crisis both largely stem from the consumption of fossil fuels. Carbon dioxide (CO_2), with its profound impact on climate, has attracted considerable attention in the past century [1–4]. With electricity supplied by renewable energy, electrochemical CO_2 reduction reaction (CO_2RR) provides an appealing route to establish a sustainable carbon cycle, which allows for storing renewable electricity as chemical feedstocks, and offers the prospect of feasible, large-scale and seasonal energy utilization [5–7]. However, CO_2 is a typically inert molecule with high dissociation energy and CO_2RR involves a lot of reaction routes and multiple proton/electron transfer steps. Moreover, CO_2RR in aqueous solution is inevitably competed by the hydrogen evolution reaction (HER). These aspects result in low selectivity and energy conversion efficiency [8–11]. Therefore, developing efficient catalysts with high activity and selectivity via structural tuning and active sites engineering are essential for CO_2 utilization [12–14].

Generally, the trade-off between energy efficiency, electron intensity, and product selectivity makes certain CO_2RR products economically more viable [15,16]. In this regard, formic acid/formate is a desirable product with high economic value and wide application in many industries [17,18]. Because of the relatively optimal adsorption capability toward key intermediate, a lot of efforts have been paid on Sn based materials to advance the CO_2-to-formate conversion technology [19–21]. Kanan's group proved that the oxide species (SnO_x) are beneficial to enhance catalytic activity and selectivity toward formate [22]. Given the unique and essential role of SnO_x, nanostructured SnO_2 was applied as alternative catalyst, which usually favors formate production over carbon monoxide and hydrogen [23–27]. However, most of these catalysts only produce formate with high faradaic efficiency (FE) in a very narrow potential window [17,28–30]. It is likely because SnO_2 tends to be reduced into metallic Sn prior to the CO_2RR according to standard redox potential, and the resulting Sn is less selective to formate [31,32]. Moreover, the proportion of Sn is significantly affected by applied potential, which leads to variation in catalytic activity and selectivity [33]. For ideal electrocatalysts, catalytic activity, selectivity and stability are all essential [34]. To this end, it is very important yet challenging to keep SnO_x stable and maintain the selectivity toward formate under CO_2RR condition, especially at very negative potentials.

In order to improve the stability of SnO_x, one of the strategies is to design more active catalytic surface for CO_2RR, because the stability of

* Corresponding author.
E-mail address: xiaoxihuang@szpt.edu.cn (X. Huang).

https://doi.org/10.1016/j.nanoen.2023.108193
Received 29 September 2022; Received in revised form 17 December 2022; Accepted 6 January 2023
Available online 8 January 2023

SnO_x is related with the competition between catalyst self-reduction and CO_2 reduction, enhancing the catalytic activity is favorable to accelerate electron transfer along the CO_2RR pathway, thereby stabilizing SnO_x species. On the other hand, surface hydroxyls were demonstrated to promote the stability of SnO_x [35], or improve the catalytic activity and selectivity [36–38]. These works are essential to understand the contributions of surface hydroxyls on metal oxides for electrocatalysis. For example, Sn branches catalysts composed of metallic Sn and 5-nm-thick amorphous $SnO_x(OH)_y$ shell were synthesized to study the role of surface hydroxyls and stability of SnO_x [35]. Another example is a Sn catalyst composed of a mixture of SnO_2, Sn_3O_4 and SnO [37]. Despite these important works, due to the complicated surface structures of composite heterogeneous materials, it is challenging to construct structure models that represent real catalyst to investigate the role of surface hydroxyls via theoretical methods. The presence of multi-phase in the catalyst also makes the monitor of structural evolution difficult during CO_2RR. To this end, more efforts are required to understand the mechanism of CO_2RR and the role of surface hydroxyls in order to design more stable electrocatalysts.

In this paper, we design a method that can synthesize tin dioxide (SnO_2-1) with abundant surface hydroxyls. And we prove that the oxide species in SnO_2-1 is more stable over the course of CO_2RR compared with the control sample, which has very few hydroxyl groups. Thanks to the presence of surface hydroxyls, SnO_2-1 exhibits high selectivity to formate at a wide potential range, and robust durability under high current density. Based on the theoretical calculations, we identify that surface hydroxyls are more difficult to remove compared with bridged oxygen atoms on SnO_2 (110) surface. Additionally, we prove that partially reduced SnO_2 (110) surface can generate a series of binding sites with more suitable free energy of formation for key intermediate *OCHO.

2. Experimental section

2.1. Synthesis of SnO_2-1 and SnO_2-2

A precursor was firstly synthesized via a co-assembly method of Na_2SnO_3 and phenolic resin. Typically, 2.0 g of phenol and 7 mL of formaldehyde (37 wt% aqueous solution) were dissolved in 50 mLof 0.1 M NaOH aqueous solution at 70 °C under stirring for 30 min. Simultaneously, 4.4 g of triblock copolymer F127 (EO106PO70EO106, Mw = 13,600) and 1.5 g $Na_2SnO_3{\cdot}3\ H_2O$ was dissolved in 50 mL DI water. These two solutions were mixed, mildly stirred at 65 °C for 72 h and then stirred for another 24 h at 70 °C. The product was collected via centrifugation, rinsed with DI water for several times and then dried at room temperature. The precursor (2.0 g) was converted into tin dioxide via thermal annealing in muffle furnace at 600 °C for 2 h with a heating rate of 5 °C/min. The corresponding sample was labeled as SnO_2-1. For comparison purpose, SnO_2-2 was synthesized using SnO_2-1 as starting material. Firstly, the as-obtained SnO_2-1 was dispersed in 0.1 M HCl aqueous solution for 20 min (or in 0.5 M $KHCO_3$ solution for 30 min). Subsequently, the solid product was collected with centrifugation and rinsed by deionized water for several times. After dried at room temperature in vacuum, the product was heated to 300 °C at the rate of 5 °C/min and kept at this temperature for 2 h. Finally, the product was collected and labeled as SnO_2-2.

2.2. Characterization

Electron microscope images and elemental mappings were obtained by transmission electron microscope (TEM, JEOL JEM 2100 F) and field emission scanning electron microscope (FESEM, Zeiss SIGMA). X-ray photoelectron spectroscopy (XPS) was performed on a ThermoFisher Nexsa X-Ray photoelectron spectrometer with Al Kα excitation source. X-ray powder diffraction (XRD) patterns were recorded on a Bruker D8 Advanced X-ray diffractometer using Cu Kα radiation source (λ = 0.15418 nm). The total concentrations of sodium in the samples were determined using an Inductively Coupled Plasma Optical Emission Spectrometer (ICP-OES, Agilent 720ES). Thermo Gravimetric Analysis was conducted in air flow on a thermal gravimetric analyzer (TA instrument, Discovery TGA 55). Temperature dependent FTIR was recorded on an Infrared Spectroscopy (PerkinElmer) and in-situ FTIR spectra was measured on Nicolet 6700 with MCT detector. Xay absorption fine structure (XAFS) spectra at Sn K (E_0 =27,940 eV) edge was acquired on the BL14W1 beamline of Shanghai Synchrotron Radiation Facility (SSRF).

2.3. Electrochemical measurements

The electrochemical measurements were performed on an electrochemical workstation (CHI 660E) using a typical three-electrode system. A Ag/AgCl (3 M KCl) electrode and a piece of platinum foil (1 × 1 cm^2) served as reference and counter electrode, respectively. Regarding to the working electrode preparation, 1 mL of ethanol and 80 μL of Nafion solution (5 wt%) was used to disperse 10 mg of electrocatalyst via ultrasonication. Subsequently, 200 μL of the uniform electrocatalyst ink was sprayed on porous conductive carbon paper (1 × 1 cm^2) and the resulting electrode was dried in a vacuum oven for 24 h at 60 ℃. Both compartments of H-cell were filled with 60 mL of 0.5 M $KHCO_3$ solution and separated by a proton exchange membrane. CO_2 gas was bubbled through the cathodic compartment before electrochemical measurement to saturate the electrolyte and the bubbling was continued during bulk electrolysis at a constant rate (10 sccm). The cathodic electrolyte was stirred at 350 rpm. Constant potential electrolysis was conducted at different potentials ranging from − 0.8 to − 1.4 V vs. RHE.

The electrochemical active surface area (ECSA) was determined by recording cyclic voltammetry (CV) curves from 0.1 to 0.3 V vs RHE at a series of scan rates. The turn over frequency is typically calculated according to the following equation:

$$\mathrm{TOF} = \frac{\mathrm{j}}{\mathrm{n} \times \mathrm{F} \times \mathrm{L}}$$

where j is the current density, n is the number of electrons transferred, F is the faraday constant and L is the amount of active sites under the assumption that all tin atoms in the catalyst are active.

Electrocatalytic performance at high current density was evaluated in a flow cell reactor. In addition to the anodic chamber and cathodic chamber, the reactor comprises a gas chamber next to the cathodic chamber, which allows CO_2 gas to pass through directly. A proton exchange membrane (Nafion 117) was used to separate the anodic and cathodic chambers. A Pt foil was assembled in anodic chamber to server as counter electrode. Carbon paper loaded with tin dioxide was used as working electrode and sandwiched between cathodic and gas chamber. A Ag/AgCl electrode was used as reference electrode. For the preparation of working electrode, 5 mg of catalysts was sprayed on 1.5 × 3 cm^2 carbon paper, and the actual geometric area exposed to cathodic electrolyte was 1 cm^2. The CO_2 electroreduction was evaluated in 1 M $KHCO_3$ or 1 M KOH electrolyte with constant 30 sccm of CO_2 gas feed.

2.4. Products analysis

The products were analyzed according to our previous reports [39,40]. Gas products were analyzed via online gas chromatography (Agilent 7890B) with an interval of 20 min during bulk electrolysis for two hours. Electrolyte was sampled after two hours of electrolysis and analyzed by nuclear magnetic resonance chemical analyzer (JEOL JEM-ECZ400S/L1).

2.5. Theoretical calculations

Density functional theory (DFT) calculations were performed with

MedeA VASP (Vienna ab-initio simulation package) [41–43]. The interactions were described by the GGA-PBE (Generalized Gradient Approximation-Perdew-Burke-Ernzerhof) exchange-correlation functional [44]. Van der Waals interactions were considered by means of a forcefield (DFT+D3 approach of S. Grimme with zero-damping) [45]. For adsorbed intermediates on catalyst slab, the Gibbs free energy calculations were performed with post-processing VASPKIT package at 298.15 K [46]. Computational hydrogen electrode (CHE) model was used to calculate the value of $G(H^+ + e^-)$ and describe the influence of applied potential [47]. The Gibbs free energies of non-adsorbed species were obtained from previous publications and the values are summarized in Table S1 [48,49]. See more details in supporting information.

3. Results and discussion

3.1. Materials synthesis and characterization

To synthesize tin dioxide electrocatalyst covered with surface hydroxyls (SnO_2-1), a tin precursor was first prepared through a co-assembly method, wherein the phenolic resins and F127 amphipathic triblock copolymers were applied as soft-templates (Fig. 1a). The precursor has roughed surface according to SEM observation (Fig. S1a). During the subsequent calcination process in air, the organic template decomposed, as evidenced by dramatic drop in weight between 250 and 400 °C in thermogravimetric curve (Fig. S1b). The resulting tin dioxide material has rutile crystal structure (Fig. S2). The corresponding SEM (Fig. S3) and TEM (Fig. 1b) images indicate that SnO_2-1 is constructed by intertwined nanoparticles. High resolution TEM image (Fig. 1b) reveals a lattice distance of 0.33 nm and 0.26 nm, corresponding to the (110) and (101) planes of SnO_2, respectively.

It should be noted that the EDS mappings demonstrate that tin, oxygen and sodium elements are uniformly distributed along the mesoporous structure (Fig. 1c), indicating some of the sodium cations are trapped inside the as-synthesized precursor during the sol-gel reaction. These sodium cations can retain in the structure of SnO_2-1 even after calcination, and this is confirmed by Na 1s XPS spectrum (Fig. 2a). The sodium cations can interact with surface oxygen atoms via ionic bonds (Sn-O-Na). When immersed in electrolyte, we speculate that the Sn-O-Na moiety could be hydrolyzed to generate surface hydroxyls as illustrated in Fig. 1a. This hypothesis is proved by XPS analysis, as the Na 1s peak

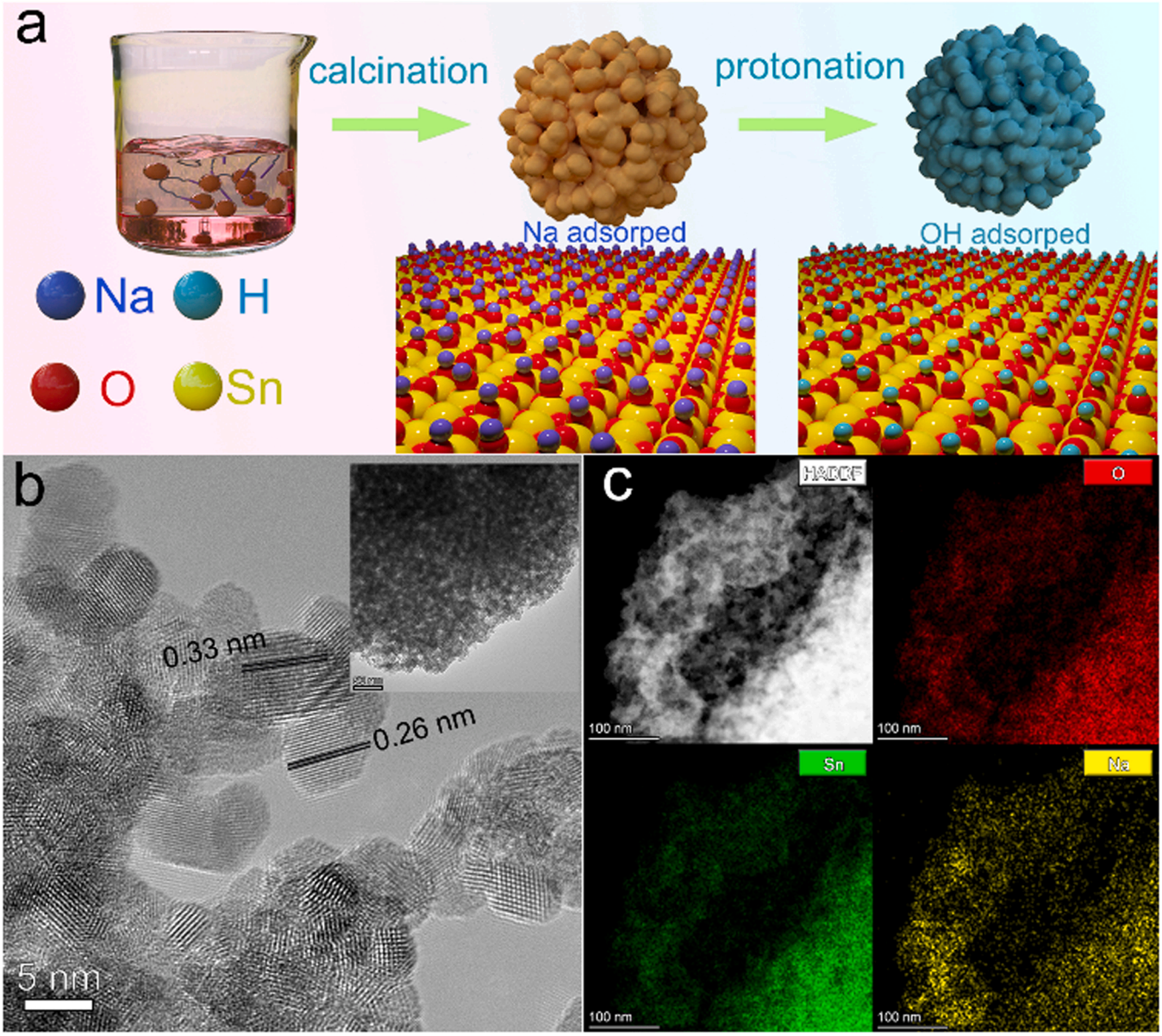

Fig. 1. Synthesis and characterization of SnO_2-1. (a) Schematic illustration of the synthesis process of SnO_2-1; (b) TEM and (c) EDS elemental mapping of SnO_2-1.

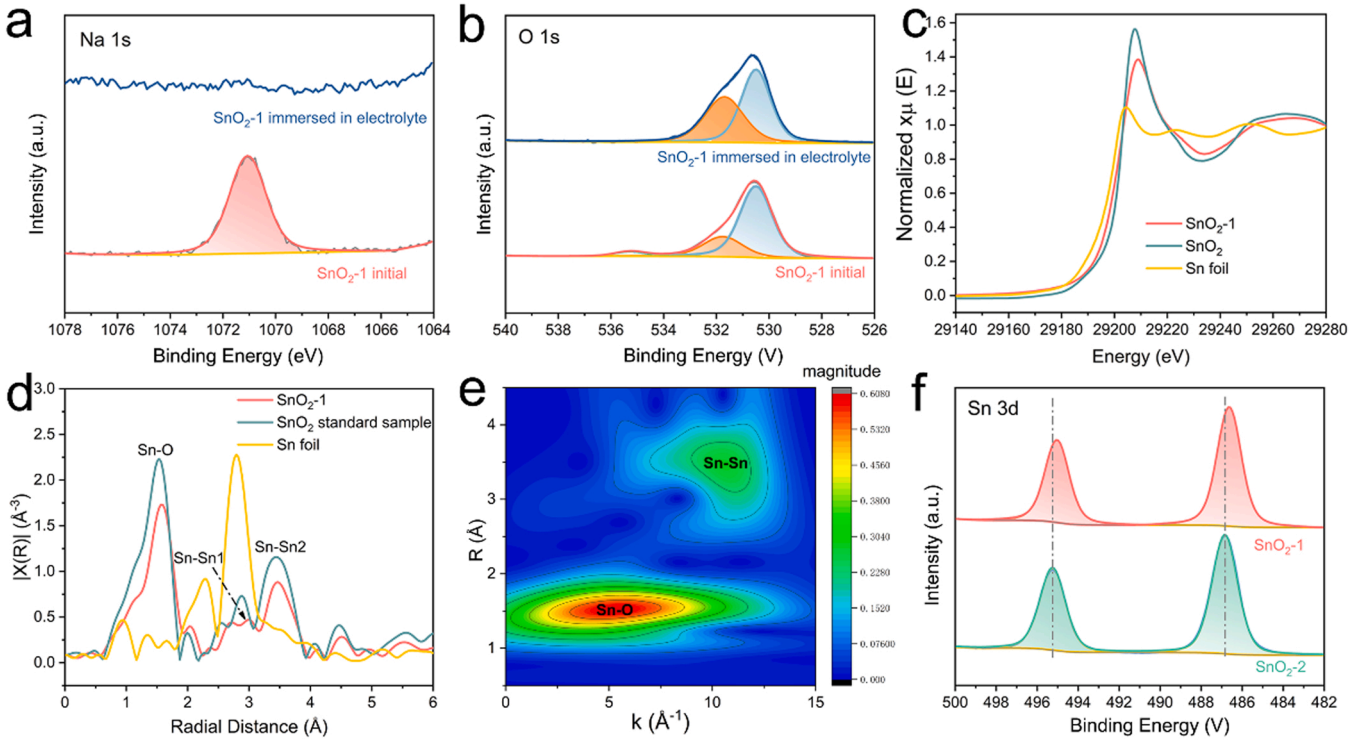

Fig. 2. XPS spectrum of (a) Na 1s and (b) O 1s before and after soaking SnO_2-1 in electrolyte; (c) Comparison of Sn K-edge XANES spectra for SnO_2-1 and reference sample. (d) The comparison of Sn K-edge EXAFS, shown in k^2 weighted *R*-space. (e) The wavelet transform of SnO_2-1. (f) Comparison of Sn 3d XPS spectrum of SnO_2-1 and SnO_2-2.

disappears after soaking SnO_2-1 with 0.5 M $KHCO_3$ electrolyte solution (Fig. 2a). Furthermore, in O 1s spectrum of SnO_2-1, the peaks at 530.5 and 531.7 eV are assigned to oxygen in oxide and hydroxide forms [35]. It seems that SnO_2-1 has higher proportion of hydroxyl species on the surface after reacting with the electrolyte (Fig. 2b). The content of hydroxyls is estimated as 43% among the total oxygen on the surface based on the integration of the peak area in O 1s XPS spectra. Similar result is obtained when the electrolyte is replaced by 0.1 M HCl solution (Fig. S4), which indicates the peaks at 531.7 eV is predominantly correlated with surface hydroxyls instead of adsorbed HCO_3^-.

In addition, the minor peak at ~536 eV associated with Na KLL becomes negligible after soaking in 0.5 M $KHCO_3$ solution [50]. Meanwhile, the sodium content decreased from 6.18% to 0.018% after soaking SnO_2-1 with 0.5 M $KHCO_3$ electrolyte solution based on ICP measurement. These results prove the formation of tin dioxide with surface Sn-O-Na functional groups that can be converted to surface hydroxyls (Sn-OH) upon interacting with aqueous electrolyte.

After soaking SnO_2-1 in the electrolyte, the presence of surface OH was further demonstrated by X-ray absorption spectroscopy (XAS) analysis (Fig. 2c–e). X-ray absorption near edge structure (XANES) profile of Sn K edge (Fig. 2c) of SnO_2-1 reveals similar peak position and shape to that of standard SnO_2, indicating the predominant phase is SnO_2. The extended X-ray absorption fine structure (EXAFS) of Sn in SnO_2-1 was analyzed, wherein Sn-O in first shell and Sn-Sn in second shell were included. The corresponding peaks were observed at 1.7 and 3.5 Å respectively in R-space fitting data (Fig. 2d). Moreover, the high lobes in the wavelet transformation result (Fig. 2e) are contributed from Sn-O and Sn-Sn without other unrelated atoms. The high lobes in the wavelet transformation results of SnO_2 reference sample are shown in Fig. S5. Based on the fitting results (Table S2), the coordination number (CN) ratios of Sn-O and Sn-Sn for SnO_2-1 and SnO_2 reference sample were estimated as ~1.1 and ~0.93, respectively. This means Sn atoms are connected with more O atoms in SnO_2-1 compared with SnO_2 reference sample, which is due to the presence of additional hydroxyl groups in SnO_2-1.

For comparison purpose, after soaking SnO_2-1 with 0.1 M HCl to protonate Sn-O-Na, the resulting sample was further annealed in air at 300 °C to remove most of the surface hydroxyls (denoted as SnO_2-2). At high temperature, the surface hydroxyls can undergo dehydration reaction; as a result, the amount of hydroxyls decreases (to ~12%) in the XPS spectrum (Fig. S6). Similar result is observed when 0.1 M HCl is replaced with 0.5 M $KHCO_3$. Meanwhile, due to the removal of sodium cations and additional annealing process, the Sn 3d of SnO_2-2 shifts to higher binding energy compared with that of SnO_2-1 (Fig. 2f). It should also be noted that the mesoporous structure is retained in SnO_2-2 after annealing process based on SEM and TEM observations (Fig. S7) and the specific surface area (15.5 $m^2 \cdot g^{-1}$) is quite comparable to that of SnO_2-1 (18.7 $m^2 \cdot g^{-1}$). Moreover, the XRD patterns of SnO_2-2 and SnO_2-1 both match the rutile crystal structure of tin dioxide (Fig. S2).

3.2. *Evaluation of electrochemical CO_2RR performance*

The catalytic performance of SnO_2-1 and SnO_2-2 for CO_2RR was evaluated in CO_2-saturated 0.5 M $KHCO_3$ within an H-cell. The selectivities were measured at various potential values between − 0.8 and − 1.4 V and the catalysts were reduced at − 0.8 V before the potentiostatic electrolysis. As depicted in Fig. 3ab, gaseous products H_2 and CO were detected for both SnO_2-1 and SnO_2-2, and formate is the only liquid product. But the selectivities are distinct between these two catalysts. Regarding SnO_2-2, the $FE_{formate}$ is apparently dependent on the applied potential values and displays a typical volcano-shaped correlation with a maximum FE reaching ~79% at − 1.1 V, while the HER becomes more dominant and $FE_{formate}$ drops considerably at potential values beyond − 1.1 V. In stark contrast, SnO_2-1 exhibits much higher $FE_{formate}$ of ~86% as maximum (Fig. 3a). Moreover, the selectivity of SnO_2-1 is not quite influenced by the operating potential, as high selectivity toward formate is obtained through a wide potential window from − 0.8 to − 1.4 V, and the FE of competing hydrogen product keeps below 20%.

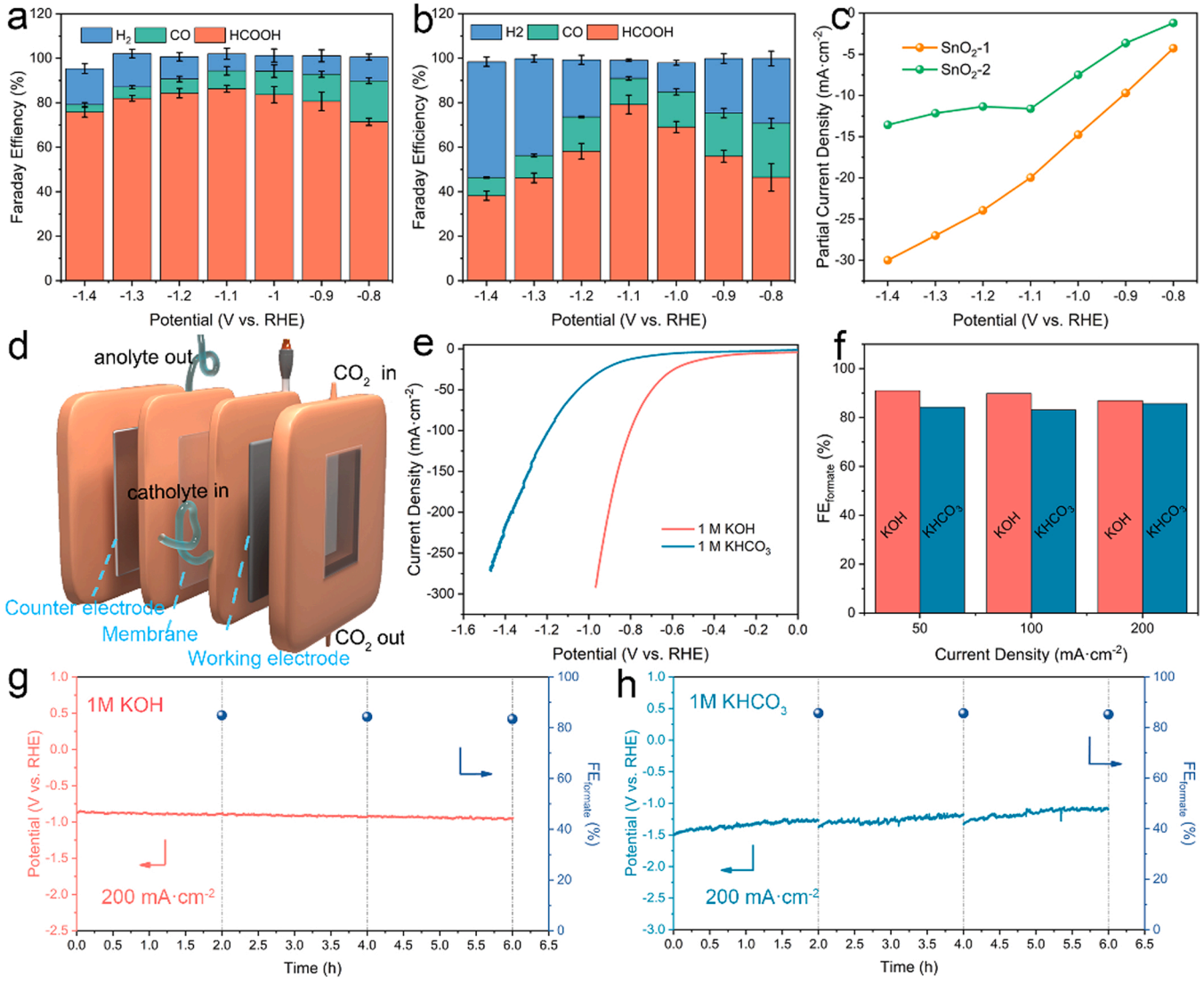

Fig. 3. CO_2RR performance of SnO_2-1 and SnO_2-2. Comparison of FE values in H-cell using 0.5 M $KHCO_3$ as electrolyte for (a) SnO_2-1 and (b) SnO_2-2, and corresponding formate partial current density (c). (d) Schematic illustration of the flow cell configuration. Comparison of (e) LSV curves and (f) $FE_{formate}$ in 1 M KOH and 1 M $KHCO_3$ in flow cell for SnO_2-1. Stability evaluation of SnO_2-1 in (g) 1 M KOH and (h) 1 M $KHCO_3$ in flow cell at 200 mA·cm^{-2}.

Such a performance is quite comparable to recently reported SnO_2 based catalysts (Fig. S8) and highly desirable when the electrolysis is driven by renewable energy supply as these energy sources are generally intermittent and unstable. Of note, the partial current density of formate (J_{HCOO-}) catalyzed by SnO_2-1 is significantly larger than that of SnO_2-2 within the voltage range of − 0.8 to − 1.4 V (Fig. 3c) despite their ECSA values are relatively close (Fig. S9). Based on the loading of catalyst, the turn-over frequency (TOF) is calculated and the TOF of SnO_2-1 is higher than that of SnO_2-2 (Fig. S10), indicating that SnO_2-1 is more active intrinsically.

The aforementioned analysis reveals more appealing catalytic properties of SnO_2-1, however, the limited solubility of CO_2 hinders the reaction rate in H-type cell. To overcome the issue of CO_2 solubility, the catalytic activity of SnO_2-1 was further evaluated in a flow cell at high current densities ranging from 50 to 200 mA·cm^{-2} (Figs. 3d–h and S11). Consistent with the performance in H-cell, SnO_2-1 exhibits remarkable selectivity toward formate at a wide range of current densities from 50 to 200 mA·cm^{-2} in both 1 M KOH and 1 M $KHCO_3$. The $FE_{formate}$ is over 80% even under current density of 200 mA·cm^{-2} and the performance is stable for at least six hours.

3.3. *Investigating the mechanism of CO_2RR*

Next we aim to understand the high selectivity of formate in wide potential range catalyzed by SnO_2-1. Generally, CO_2RR is operated under negative cathodic potential in order to activate stable CO_2 and increase the production rate of desired products. Under this condition, SnO_2 is thermodynamically unstable and has a tendency to undergo electrochemical self-reduction according to the Pourbaix diagram [31]. In our case, a telltale sign of catalyst structural reconstruction is the change of color at the early stage of electrolysis, which is accompanied by the change of corresponding current densities (Fig. S12). To uncover the details of structural evolution, XRD of the electrode was measured after CO_2RR. At the potential of − 0.8 V, the XRD patterns reveal that proportion of metallic Sn in SnO_2-1 remains negligible despite the reducing process was continued for 2 h (Fig. S13a). On the contrary, clear peaks associated with metallic Sn were observed in SnO_2-2 after 2 h of reduction (Fig. S13b). When the cathodic potential was further reduced to − 1.1 V, the increase of metallic Sn in SnO_2-2 was even more pronounced compared with that in SnO_2-1, suggesting that SnO_2-1 is more stable and can tolerate reduction condition in CO_2RR. The high selectivity toward formate in wide potential window is rationally

correlated with different amounts of metallic Sn generated under CO_2RR condition. Noting that the selectivity of pure metallic tin is poor toward formate in CO_2RR [22], the decreased $FE_{formate}$ of SnO_2-2 at very negative potential is likely due to the formation of too much metallic tin.

The surface hydroxyls are detectable in XPS spectra after the electrochemical measurement (Fig. S14). To understand the role of surface hydroxyls on the stability and catalytic performance of CO_2RR, the SnO_2 (110) surface was adopted as the model for theoretical calculations, since it is the relatively more stable surface [51]. On the 2x2 surface, there are four bridged oxygen (Obri) atoms, and two types of tin, namely Sn5c and Sn6c, respectively coordinated with 5 and 6 oxygen atoms (Fig. S15). The electrochemical conversion of tin oxide to metallic tin may start from reductive elimination of oxygen species on the surface of catalyst. Under the applied negative potential, the surface can be reduced to create several oxygen vacancies. Starting from the stoichiometric SnO_2 (110) surface, we first calculate the free energy changes (ΔGs) of reducing one, two, three and four Obri atoms, namely leaving 75%, 50%, 25% and 0% of Obri atoms on the surface (Fig. 4a). Computational hydrogen electrode (CHE) model was used to describe the influence of electrode potential and the results are shown at − 0.8 V vs. RHE. In terms of 50% coverage of surface Obri, there are three circumstances, which are denoted as Obri_50%a, Obri_50%b, Obri_50%c. It is clear that the ΔGs are very negative for the successive introduction of Obri vacancies (Fig. 4a), indicating that reductive elimination of Obri is thermodynamically favorable. In contrast, when the surface is covered with all bridged OH (OHbri, Fig. 4b), the ΔGs for removing OHbri moiety fluctuate around zero and the first two steps even have slightly positive values, suggesting that the surface hydroxyl groups are difficult to remove and thus may endow the material with better stability at negative potentials. Aside from the calculations performed in vacuum, similar calculations were conducted by using implicit solvent model. The exact values of ΔG vary a little, but the overall trend remains the same compared with the results obtained in vacuum (Fig. S16). These results are consistent with the aforementioned experimental data showing that SnO_2-1 is more stable under cathodic condition due to the presence of surface hydroxyls.

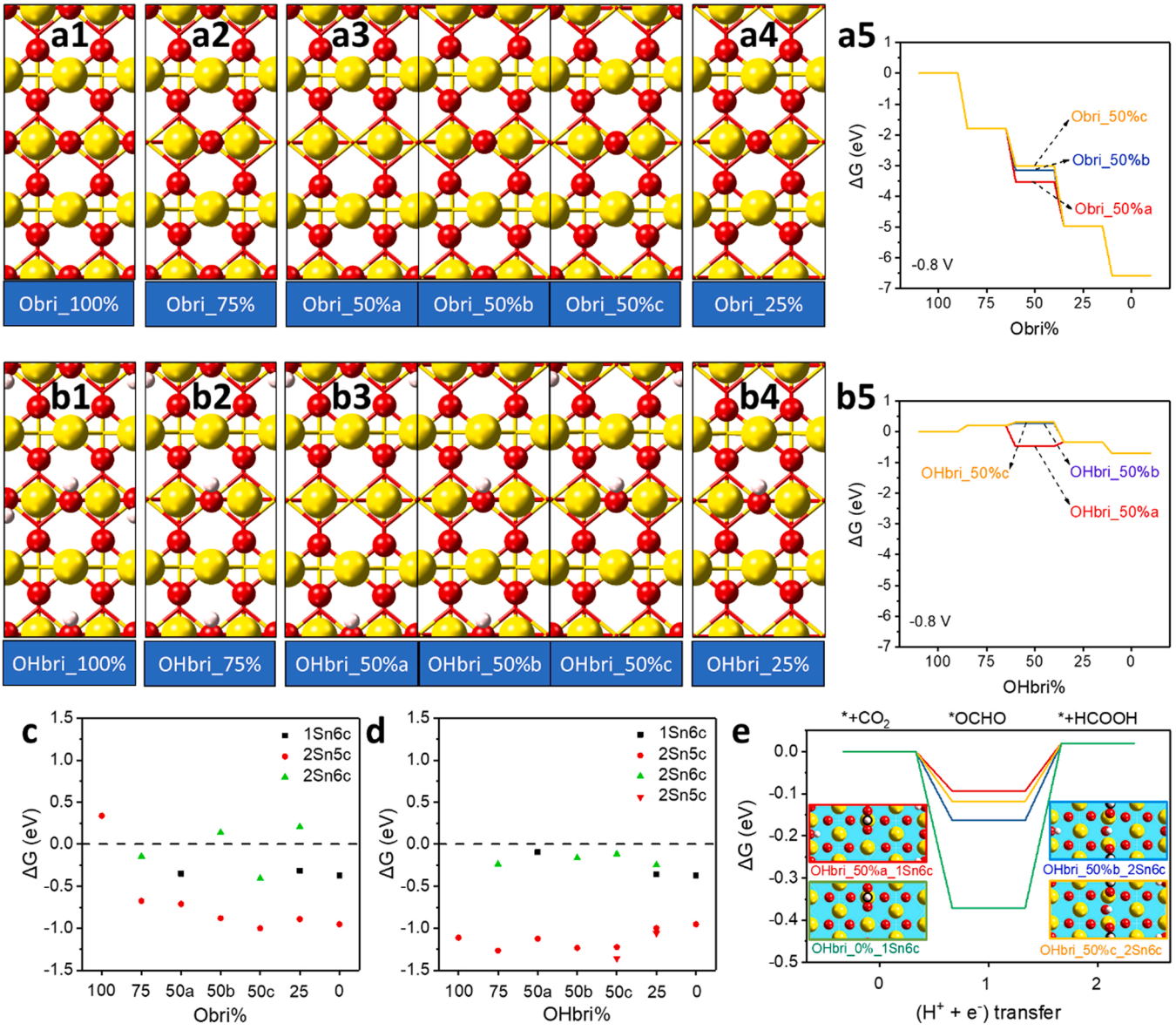

Fig. 4. DFT calculations. Optimized slab structures of SnO_2 (110) covered with different proportions of Obri (a1-a4), and OHbri (b1-b4). Corresponding change of Gibbs free energies (ΔGs) when generating partially reduced SnO_2 (110) covered with various amounts of Obri (a5) and OHbri (b5) at − 0.8 V vs. RHE. ΔG for *OCHO generation on the surface of SnO_2 (110) with different (c) Obri and (d) OHbri coverage at 0 V. (e) Comparison of ΔGs for formate production on fully reduced SnO_2 (110) and 50% OHbri covered SnO_2 (110) at 0 V.

We then evaluated the ΔG for the formation of *OCHO after one ($H^+ + e^-$) transfer step, because this is the key step for the production of formate in CO_2RR [52]. Three different adsorption configurations of *OCHO are considered, namely binding with 1Sn6c, 2Sn5c and 2Sn6c, respectively (Fig. S17). The optimized structures of *OCHO adsorption on different slabs are shown in Figs. S18 and S19. Apart from the surface of Obri_100%, it is obvious that the sites of 2Sn5c on all the surfaces bind with OCHO very strongly, indicating that the second ($H^+ + e^-$) transfer step will be difficult. Compared with fully reduced surface (Obri or OHbri_0%), partially reduced surfaces comprise of more suitable sites with optimized ΔG to produce *OCHO, especially for the series of different OHbri covered surfaces (Fig. 4cd). This result is also confirmed by the DFT calculation performed with implicit solvent model (Fig. S20). Specifically, the 1Sn6c site on OHbri_0% surface has larger energy barrier from *OCHO to HCOOH compared with other surfaces covered by 50% OHbri (Fig. 4e), indicating that partially reduced SnO_2 (110) surface has more active sites for CO_2RR. Furthermore, the ΔGs of *H formation on a variety of sites on SnO_2 (110) surface with 50% hydroxyl coverage were calculated (Fig. S21). It is obvious that all the sites have positive values for ΔG (*H), indicating that the catalyst is more selective to produce formate rather than hydrogen gas. Besides the calculations performed on SnO_2 (110) surface, the free energy change from CO_2 to formate on stoichiometric SnO_2 (101) surface (Fig. S22). The ΔG value of *OCHO formation equals 0.60 eV, slightly higher than that on stoichiometric SnO_2 (110), indicating that the difference of peak intensities in XRD in Fig. S2 is not the primary reason that govern the CO_2RR performance of SnO_2-1 and SnO_2-2. In summary, the DFT calculations predict that introducing hydroxyl groups on the surface of SnO_2 can not only improve the stability, but also promote the CO_2-to-formate conversion rate by optimizing the ΔG of *OCHO formation.

Of the DFT calculated results in Fig. 4d, it is apparent that the surface of SnO_2-1 can exist in the form of partially reduced state with sites that can produce *OCHO with optimized ΔG. Binding sites like 1Sn6c and 2Sn6c have more suitable ΔG to generate key intermediate *OCHO. However, strong binding site of 2Sn5c is also present on these partially reduced SnO_2 (110) surface, leading to a higher energy barrier toward formate formation. If Sn5c is already connected with a terminal hydroxyl, this unfavorable strong binding site could be blocked. Temperature dependent FTIR measurement of SnO_2-1 reveals a clear peak at ~1250 cm^{-1}, due to the presence of terminal hydroxyl groups [53], and this signal is not observed in SnO_2-2 (Figs. S23 and 5ab). Moreover, the FTIR spectra (Fig. S24) collected after CO_2RR indicates that the terminal hydroxyl groups still exist in SnO_2-1. It should be noted that bridged hydroxyl could be produced after one ($H^+ + e^-$) reduction from bridged oxygen when applying negative potential [54], however, the terminal hydroxyl could not be produced in this way. Therefore, we further performed DFT calculations to illustrate the influence of terminal hydroxyl groups on CO_2RR performance. Starting from the slab of OHbri_50%c, the 2Sn6c site has nearly optimal ΔG for the production of formate, but the strong binding sites of 2Sn5c are undesired (Fig. 5c). We then added terminal hydroxyls with 50% coverage on this surface and calculated the free energy diagram for CO_2 to formate conversion (Fig. 5d). One of the 2Sn6c sites still binds with OCHO weakly, resulting in lowest energy barriers for HCOOH production, while another 2Sn6c site binds with OCHO with medium strength, due to the hydrogen bond formed between OCHO and terminal hydroxyls (Fig. 5d, blue curve). More importantly, the occupation of terminal hydroxyl at Sn5c changes the bidentate binding mode of 2Sn5c to monodentate binding mode of 1Sn5c with more optimized ΔG for *OCHO generation, and it is likely to accelerate the next ($H^+ + e^-$) transfer step. These results suggest that aside from the contribution from partially reduced surface, the presence of terminal hydroxyls is another factor that can improve the catalytic

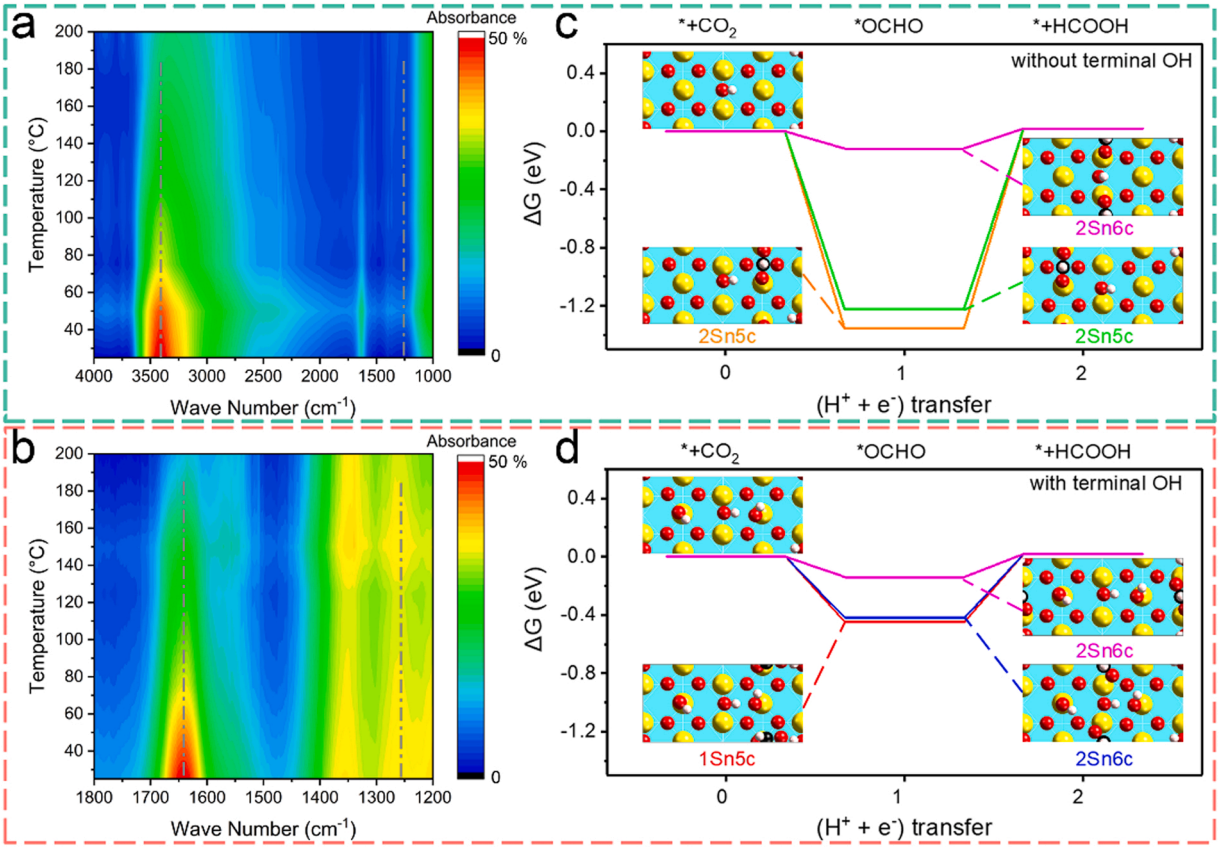

Fig. 5. Comparison of CO_2RR activity on SnO_2 with and without terminal OH. Temperature dependent FTIR spectra of (a) SnO_2-2 and (b) SnO_2-1. DFT calculated theoretical energy diagrams of SnO_2 (110) surface (c) without terminal OH and (d) with terminal OH.

activity. At last, in-situ FTIR was performed to probe the existence of possible intermediate during CO_2RR (Fig. S25). A signal at ca. 1400 cm^{-1} is observed, due to the formation of *OCHO intermediate, which is in agreement with the DFT calculations [55].

4. Conclusion

In summary, we synthesized a tin dioxide electrocatalyst via sodium cation assisted calcination method. The surface of as-obtained SnO_2-1 is covered with plenty of hydroxyls, which help to maintain its stability under CO_2RR condition and construct active sites for efficient CO_2-to-formate conversion. Compared with SnO_2-2, which has minimal amount of surface hydroxyls, SnO_2-1 delivers a superior catalytic performance with a high $FE_{formate}$ (> 80%) over a wide potential range, as well as a high partial current density. Moreover, SnO_2-1 exhibits remarkable performance in flow cell with high selectivity and robust stability. The catalytic mechanism underlying these tin dioxides as well as their stabilization mechanisms were uncovered. Taking the DFT calculations and the experimental results together, we provide a plausible explanation for the improved selectivity and stability of CO_2-to-formate conversion on tin dioxide. This study opens up exciting new avenues to develop efficient SnO_2 based catalysts with outstanding performance for CO_2 conversion applications.

CRediT authorship contribution statement

Zhipeng Liu: Methodology, Investigation, Data curation, Writing – original draft. **Junjie Chen:** Methodology. **Hongshan Guo:** Validation. **Xiaoxi Huang:** Conceptualization, Writing – original draft, Supervision, Funding acquisition, Investigation.

Declaration of Competing Interest

The authors declare that they have no known competing financial interests or personal relationships that could have appeared to influence the work reported in this paper.

Data availability

Data will be made available on request.

Acknowledgments

This work was supported by the Guangdong Natural Science Foundation (2022A1515110034) and Innovation Team Project of Guangdong (2022KCXTD055), the Scientific and Technical Innovation Council of Shenzhen (Task Book No. GXWD20201231165806004, Project No. 20200828014156001), and we also thank the support from Shenzhen Polytechnic.

Appendix A. Supplementary material

Supplementary data associated with this article can be found in the online version at doi:10.1016/j.nanoen.2023.108193.

References

[1] L. Fan, C. Xia, F. Yang, J. Wang, H. Wang, Y. Lu, Strategies in catalysts and electrolyzer design for electrochemical CO_2 reduction toward C2+ products, Sci. Adv. 6 (2020) EAAY3111.
[2] P. De Luna, C. Hahn, D. Higgins, S.A. Jaffer, T.F. Jaramillo, E.H. Sargent, What would it take for renewably powered electrosynthesis to displace petrochemical processes? Science 364 (2019) eaav3506.
[3] S. Jin, Z. Hao, K. Zhang, Z. Yan, J. Chen, Advances and challenges for the electrochemical reduction of CO_2 to CO: from fundamentals to industrialization, Angew. Chem. Int. Ed. 60 (2021) 20627–20648.
[4] J. Artz, T.E. Muller, K. Thenert, J. Kleinekorte, R. Meys, A. Sternberg, A. Bardow, W. Leitner, Sustainable conversion of carbon dioxide: an integrated review of catalysis and life cycle assessment, Chem. Rev. 118 (2018) 434–504.
[5] G. Wang, J. Chen, Y. Ding, P. Cai, L. Yi, Y. Li, C. Tu, Y. Hou, Z. Wen, L. Dai, Electrocatalysis for CO_2 conversion: from fundamentals to value-added products, Chem. Soc. Rev. 50 (2021) 4993–5061.
[6] F. Pan, Y. Yang, Designing CO_2 reduction electrode materials by morphology and interface engineering, Energy Environ. Sci. 13 (2020) 2275–2309.
[7] R.I. Masel, Z. Liu, H. Yang, J.J. Kaczur, D. Carrillo, S. Ren, D. Salvatore, C. P. Berlinguette, An industrial perspective on catalysts for low-temperature CO_2 electrolysis, Nat. Nanotechnol. 16 (2021) 118–128.
[8] C. Long, X. Li, J. Guo, Y. Shi, S. Liu, Z. Tang, Electrochemical reduction of CO_2 over heterogeneous catalysts in aqueous solution: recent progress and perspectives, Small Methods (2018), 1800369.
[9] P. Saha, S. Amanullah, A. Dey, Selectivity in electrochemical CO_2 reduction, Acc. Chem. Res. 55 (2022) 134–144.
[10] A. Liu, M. Gao, X. Ren, F. Meng, Y. Yang, L. Gao, Q. Yang, T. Ma, Current progress in electrocatalytic carbon dioxide reduction to fuels on heterogeneous catalysts, J. Mater. Chem. A 8 (2020) 3541–3562.
[11] S. Liu, X.F. Lu, J. Xiao, X. Wang, X.W.D. Lou, Bi_2O_3 nanosheets grown on multi-channel carbon matrix to catalyze efficient CO_2 electroreduction to HCOOH, Angew. Chem. Int. Ed. 58 (2019) 13828–13833.
[12] L. Dai, Q. Qin, P. Wang, X. Zhao, C. Hu, P. Liu, R. Qin, M. Chen, D. Ou, C. Xu, S. Mo, B. Wu, G. Fu, P. Zhang, N. Zheng, Ultrastable atomic copper nanosheets for selective electrochemical reduction of carbon dioxide, Sci. Adv. 3 (2017), e1701069.
[13] J. Wang, S. Dou, X. Wang, Structural tuning of heterogeneous molecular catalysts for electrochemical energy conversion, Sci. Adv. 7 (2021) eabf3989.
[14] H. Zhang, X. Jin, J.M. Lee, X. Wang, Tailoring of active sites from single to dual atom sites for highly efficient electrocatalysis, ACS Nano 16 (2022) 17572–17592.
[15] O.S. Bushuyev, P. De Luna, C.T. Dinh, L. Tao, G. Saur, J. van de Lagemaat, S. O. Kelley, E.H. Sargent, What should we make with CO_2 and how can we make it? Joule 2 (2018) 825–832.
[16] K. Ye, Z. Zhou, J. Shao, L. Lin, D. Gao, N. Ta, R. Si, G. Wang, X. Bao, In situ reconstruction of a hierarchical Sn-Cu/SnO_x core/shell catalyst for high-performance CO_2 electroreduction, Angew. Chem. Int. Ed. 59 (2020) 4814–4821.
[17] N. Han, P. Ding, L. He, Y. Li, Y. Li, Promises of main group metal–based nanostructured materials for electrochemical CO_2 reduction to formate, Adv. Energy Mater. 10 (2019), 1902338.
[18] Y. Guan, M. Liu, X. Rao, Y. Liu, J. Zhang, Electrochemical reduction of carbon dioxide (CO_2): bismuth-based electrocatalysts, J. Mater. Chem. A 9 (2021) 13770–13803.
[19] Y.F. Tay, Z.H. Tan, Y. Lum, Engineering Sn-based catalytic materials for efficient electrochemical CO_2 reduction to formate, ChemNanoMat 7 (2021) 380–391.
[20] S. Zhao, S. Li, T. Guo, S. Zhang, J. Wang, Y. Wu, Y. Chen, Advances in Sn-based catalysts for electrochemical CO_2 reduction, Nano-Micro Lett. 11 (2019) 62.
[21] Y. Wei, J. Liu, F. Cheng, J. Chen, Mn-doped atomic SnO_2 layers for highly efficient CO_2 electrochemical reduction, J. Mater. Chem. A 7 (2019) 19651–19656.
[22] Y. Chen, M.W. Kanan, Tin oxide dependence of the CO_2 reduction efficiency on tin electrodes and enhanced activity for tin/tin oxide thin-film catalysts, J. Am. Chem. Soc. 134 (2012) 1986–1989.
[23] F. Li, L. Chen, G.P. Knowles, D.R. MacFarlane, J. Zhang, Hierarchical mesoporous SnO_2 nanosheets on carbon cloth: a robust and flexible electrocatalyst for CO_2 reduction with high efficiency and selectivity, Angew. Chem. Int. Ed. 56 (2017) 505–509.
[24] S. Liu, J. Xiao, X.F. Lu, J. Wang, X. Wang, X.W.D. Lou, Efficient electrochemical reduction of CO_2 to HCOOH over sub-2 nm SnO_2 quantum wires with exposed grain boundaries, Angew. Chem. Int. Ed. 58 (2019) 8499–8503.
[25] L.-P. Yuan, W.-J. Jiang, X.-L. Liu, Y.-H. He, C. He, T. Tang, J. Zhang, J.-S. Hu, Molecularly engineered strong metal oxide–support interaction enables highly efficient and stable CO_2 electroreduction, ACS Catal. 10 (2020) 13227–13235.
[26] L. Fan, Z. Xia, M. Xu, Y. Lu, Z. Li, 1D SnO_2 with wire-in-tube architectures for highly selective electrochemical reduction of CO_2 to C1Products, Adv. Funct. Mater. 28 (2018), 1706289.
[27] Z. Li, A. Cao, Q. Zheng, Y. Fu, T. Wang, K.T. Arul, J.L. Chen, B. Yang, N.M. Adli, L. Lei, C.L. Dong, J. Xiao, G. Wu, Y. Hou, Elucidation of the synergistic effect of dopants and vacancies on promoted selectivity for CO_2 electroreduction to formate, Adv. Mater. 33 (2021), e2005113.
[28] M. Chen, S. Wan, L. Zhong, D. Liu, H. Yang, C. Li, Z. Huang, C. Liu, J. Chen, H. Pan, D.S. Li, S. Li, Q. Yan, B. Liu, Dynamic restructuring of Cu-doped SnS_2 nanoflowers for highly selective electrochemical CO_2 reduction to formate, Angew. Chem. Int. Ed. 60 (2021) 26233–26237.
[29] S. Zhang, P. Kang, T.J. Meyer, Nanostructured tin catalysts for selective electrochemical reduction of carbon dioxide to formate, J. Am. Chem. Soc. 136 (2014) 1734–1737.
[30] Y. Yiliguma, Z. Wang, C. Yang, A. Guan, L. Shang, A.M. Al-Enizi, L. Zhang, G. Zheng, Sub-5 nm SnO_2 chemically coupled hollow carbon spheres for efficient electrocatalytic CO_2 reduction, J. Mater. Chem. A 6 (2018) 20121–20127.
[31] A. Dutta, A. Kuzume, V. Kaliginedi, M. Rahaman, I. Sinev, M. Ahmadi, B. Roldán Cuenya, S. Vesztergom, P. Broekmann, Probing the chemical state of tin oxide NP catalysts during CO_2 electroreduction: a complementary operando approach, Nano Energy 53 (2018) 828–840.
[32] S. Lee, J.D. Ocon, Y.-I. Son, J. Lee, Alkaline CO_2 electrolysis toward selective and continuous HCOO– production over SnO_2 nanocatalysts, J. Phys. Chem. C 119 (2015) 4884–4890.

[33] A. Dutta, A. Kuzume, M. Rahaman, S. Vesztergom, P. Broekmann, monitoring the chemical state of catalysts for CO_2 electroreduction: an in operando study, ACS Catal. 5 (2015) 7498–7502.
[34] Y. Li, X.F. Lu, S. Xi, D. Luan, X. Wang, X.W.D. Lou, Synthesis of N-doped highly graphitic carbon urchin-like hollow structures loaded with single-Ni atoms towards efficient CO_2 electroreduction, Angew. Chem. Int. Ed. 61 (2022), e202201491.
[35] W. Deng, L. Zhang, L. Li, S. Chen, C. Hu, Z.J. Zhao, T. Wang, J. Gong, Crucial role of surface hydroxyls on the activity and stability in electrochemical CO_2 reduction, J. Am. Chem. Soc. 141 (2019) 2911–2915.
[36] X.-C. Liu, C. Wei, Y. Wu, Y. Fang, W.-Q. Li, R.-R. Ding, G. Wang, Y. Mu, Tailoring the electrochemical protonation behavior of CO_2 by tuning surface noncovalent interactions, ACS Catal. 11 (2021) 14986–14994.
[37] J. Li, J. Li, X. Liu, J. Chen, P. Tian, S. Dai, M. Zhu, Y.-F. Han, Probing the role of surface hydroxyls for Bi, Sn and In catalysts during CO_2 reduction, Appl. Catal. B 298 (2021), 120581.
[38] M.F. Baruch, J.E. Pander, J.L. White, A.B. Bocarsly, Mechanistic insights into the reduction of CO_2 on tin electrodes using in situ ATR-IR spectroscopy, ACS Catal. 5 (2015) 3148–3156.
[39] J. Zhang, Z. Liu, H. Guo, H. Lin, H. Wang, X. Liang, H. Hu, Q. Xia, X. Zou, X. Huang, Selective, stable production of ethylene using a pulsed Cu-based electrode, ACS Appl. Mater. Interfaces 14 (2022) 19388–19396.
[40] Z. Liu, J. Zhang, L. Yu, H. Wang, X. Huang, Thermal derived bismuth nanoparticles on nitrogen-doped carbon aerogel enable selective electrochemical production of formate from CO_2, J. CO_2 Util. 61 (2022), 102031.
[41] G. Kresse, J. Furthmüller, Efficient iterative schemes for ab initio total-energy calculations using a plane-wave basis set, Phys. Rev. B 54 (1996) 11169–11186.
[42] G. Kresse, J. Furthmüller, Efficiency of ab-initio total energy calculations for metals and semiconductors using a plane-wave basis set, Comput. Mater. Sci. 6 (1996) 15–50.
[43] G. Kresse, D. Joubert, From ultrasoft pseudopotentials to the projector augmented-wave method, Phys. Rev. B 59 (1999) 1758–1775.
[44] J.P. Perdew, K. Burke, M. Ernzerhof, Generalized gradient approximation made simple, Phys. Rev. Lett. 77 (1996) 3865–3868.
[45] S. Grimme, J. Antony, S. Ehrlich, H. Krieg, A consistent and accurate ab initio parametrization of density functional dispersion correction (DFT-D) for the 94 elements H-Pu, J. Chem. Phys. 132 (2010), 154104.
[46] V. Wang, N. Xu, J.-C. Liu, G. Tang, W.-T. Geng, VASPKIT: a user-friendly interface facilitating high-throughput computing and analysis using VASP code, Comput. Phys. Commun. 267 (2021), 108033.
[47] A.A. Peterson, F. Abild-Pedersen, F. Studt, J. Rossmeisl, J.K. Nørskov, How copper catalyzes the electroreduction of carbon dioxide into hydrocarbon fuels, Energy Environ. Sci. 3 (2010) 1311–1315.
[48] L. Li, A. Ozden, S. Guo, Ad.A.F.P. Garci, C. Wang, M. Zhang, J. Zhang, H. Jiang, W. Wang, H. Dong, D. Sinton, E.H. Sargent, M. Zhong, Stable, active CO_2 reduction to formate via redox-modulated stabilization of active sites, Nat. Commun. 12 (2021) 5223.
[49] A. Klinkova, P. De Luna, C.-T. Dinh, O. Voznyy, E.M. Larin, E. Kumacheva, E. H. Sargent, Rational design of efficient palladium catalysts for electroreduction of carbon dioxide to formate, ACS Catal. 6 (2016) 8115–8120.
[50] G.F. Moreira, E.R. Peçanha, M.B.M. Monte, L.S. Leal Filho, F. Stavale, XPS study on the mechanism of starch-hematite surface chemical complexation, Miner. Eng. 110 (2017) 96–103.
[51] M. Batzill, U. Diebold, The surface and materials science of tin oxide, Prog. Surf. Sci. 79 (2005) 47–154.
[52] J.T. Feaster, C. Shi, E.R. Cave, T. Hatsukade, D.N. Abram, K.P. Kuhl, C. Hahn, J. K. Nørskov, T.F. Jaramillo, Understanding selectivity for the electrochemical reduction of carbon dioxide to formic acid and carbon monoxide on metal electrodes, ACS Catal. 7 (2017) 4822–4827.
[53] A.S. Tselesh, Anodic behaviour of tin in citrate solutions: the IR and XPS study on the composition of the passive layer, Thin Solid Films 516 (2008) 6253–6260.
[54] L. Li, Z.-J. Zhao, C. Hu, P. Yang, X. Yuan, Y. Wang, L. Zhang, L. Moskaleva, J. Gong, Tuning oxygen vacancies of oxides to promote electrocatalytic reduction of carbon dioxide, ACS Energy Lett. 5 (2020) 552–558.
[55] Y. Cheng, J. Hou, P. Kang, Integrated capture and electroreduction of flue gas CO_2 to formate using amine functionalized SnO_x nanoparticles, ACS Energy Lett. 6 (2021) 3352–3358.

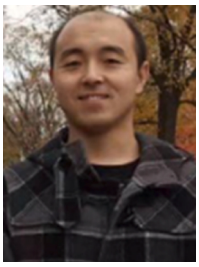

Zhipeng Liu received his MS and Ph.D degree in School of Material Science and Engineering, Jilin University. He is currently a postdoc at Shenzhen Institutes of Advanced Technology, Chinese Academy of Science and Hoffmann Institute of Advanced Materials. His current research focuses on design of catalyst materials for clean energy conversion reactions, especially the electrochemical CO_2 reduction reaction.

Junjie Chen received his B.Sc. degree in the College of Chemistry at Jilin University in 2019. Then, he started his Ph.D study in the College of Chemistry at Jilin University. His research focuses on the application of surface-enhanced Raman scattering (SERS) spectroscopy in photo-/electro-catalytic reactions, aiming at establishing a non-destructive in-situ/operando characterization platform for revealing the real active sites and key intermediates and elucidating reaction mechanisms.

Hongshan Guo received his BSc (chemistry/materials science) and MEng (sustainable energy) degrees from University of Toronto in 2016 and 2019, respectively. His research experiences include: synthesis+fabrication of nanocrystalline photocatalysts, chemical-mechanical polishing of sapphire lens, design of SOFC support layers and tape casting slurry optimization. He is currently a research assistant in Prof. Xiaoxi Huang's group at HIAM, working on synthesis of electrocatalysts and electrochemical reduction of CO_2 and O_2; he also undertakes certain lab management at HIAM.

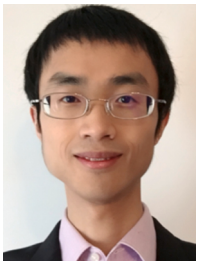

Xiaoxi Huang is an Associate Professor in Hoffmann Institute of Advanced Materials, Shenzhen Polytechnic of China. He received his Ph.D degree at Department of Chemistry and Chemical Biology from Rutgers, the State University of New Jersey in 2016. After that he joined Department of Chemistry at Purdue University as Postdoc Research Associate. Currently, his main research is focused on electrocatalysis, including CO_2 reduction, water splitting and oxygen reduction reactions.